Thin infrared imaging systems through multichannel sampling

Mohan Shankar,[1,*] Rebecca Willett,[1] Nikos Pitsianis,[1] Timothy Schulz,[2] Robert Gibbons,[3] Robert Te Kolste,[4] James Carriere,[4] Caihua Chen,[5] Dennis Prather,[5] and David Brady[1]

[1]Fitzpatrick Institute for Photonics, Duke University, Durham, North Carolina 27708, USA
[2]Department of Electrical and Computer Engineering, Michigan Technological University, Houghton, Michigan 49931, USA
[3]Raytheon Company, McKinney, Texas 75071, USA
[4]Tessera North America, Charlotte, North Carolina 28262, USA
[5]Department of Electrical and Computer Engineering, University of Delaware, Newark, Delaware 19716, USA

*Corresponding author: ms80@duke.edu

The size of infrared camera systems can be reduced by collecting low-resolution images in parallel with multiple narrow-aperture lenses rather than collecting a single high-resolution image with one wide-aperture lens. We describe an infrared imaging system that uses a three-by-three lenslet array with an optical system length of 2.3 mm and achieves Rayleigh criteria resolution comparable with a conventional single-lens system with an optical system length of 26 mm. The high-resolution final image generated by this system is reconstructed from the low-resolution images gathered by each lenslet. This is accomplished using superresolution reconstruction algorithms based on linear and nonlinear interpolation algorithms. Two implementations of the ultrathin camera are demonstrated and their performances are compared with that of a conventional infrared camera.   © 2008 Optical Society of America
    OCIS codes: 110.1758, 100.6640.

1. Introduction

Conventional imaging systems use a single-axis lens system to form an image of the scene on the focal plane. The focal resolution of the optical system (for diffraction-limited systems) depends on the wavelength and the f number, whereas the angular resolution depends on the wavelength and the entrance pupil diameter. A simple reduction in the effective focal length of the lens (keeping the f number the same) would result in a reduction in the thickness of the optical system with the disadvantage of poorer angular resolution. The focal resolution, however, remains unaffected by this reduction. This phenomenon suggests the possibility of recovering the lost angular resolution by collecting multiple images of the scene. Considerable work has been done to miniaturize the size of imaging systems by mimicking the small imaging systems that are implemented in na-

ture, for example, the compound eyes of insects [1–4]. A particular implementation of thin cameras using multiple microlenses was called the thin observation module by bound optics (TOMBO), proposed by Tanida *et al.* [5]. The cameras were designed to operate in the visible wavelength range. The system relies on the difference in sampling phase of the optical system in each subaperture to obtain nonredundant information. High-resolution images were reconstructed from the low-resolution images by various techniques, including iterative backprojection [6]. The TOMBO camera design illustrates the fact that reduction in the thickness of the optical system could be obtained using this concept. More recently, Kanaev *et al.* [7] developed a multiaperture imaging system simulator to test different optical components and reconstruction algorithms, as well as to analyze the limits of the performance of these systems.

Reduction in size and cost of long-wave infrared (LWIR) cameras has not been extensively pursued because of their limited set of applications—typically military, security, and industrial process control ap-

plications. However, smaller, lighter, and inexpensive optical systems would lower the cost of the cameras and replace the bulkier and more expensive ones that are currently used. Dowski and Kubala [8] demonstrated the reduction of cost and size of IR imaging systems by use of a technique called wavefront coding. Using this technique, they designed and fabricated a single-lens conformal LWIR imaging system by optimizing the optics and signal processing and used an appropriate wavefront code instead of a two-lens system that would have been necessary to achieve the required performance. A reduction in the form factor of IR cameras could also be obtained by using a concept similar to the TOMBO system by use of a microlens array with short focal lengths; the multiple low-resolution images that are obtained are used to reconstruct a higher-resolution image.

We have designed and developed two versions of multichannel LWIR cameras for the 9–11 μm wavelength range. One system implements a design similar to a 3 × 3 TOMBO system, with each of the lenslets displaced by a different (known) amount to obtain nonredundant information to aid in the image reconstruction. In the other system, we add a phase grating array to modulate the point-spread functions (PSFs) in each of the channels of the TOMBO system. We refer to this system as the coded PSF system. Since these cameras operate in the infrared, the microlens arrays could be fabricated with stardard silicon wafer processing techniques, which are inexpensive, favoring lower system weight as well as cost. Also, we have developed different algorithms to reconstruct a high-resolution image from the multiple low-resolution images and observe the performance of these multichannel cameras compared with a conventional infrared camera. With these systems, we demonstrate a reduction of optical system length by a factor of more than 10.

2. Optical System Design

Our approach is to replace the conventional single-channel imaging system with a multichannel imaging system. Each of the channels would have the required system f number (matching that of the conventional camera) but with a shorter effective focal length. This reduction in the effective focal length would result in the loss of system angular resolution, but the resolution is recovered from the images obtained by the multiple optical channels.

In our multichannel implementations, the aperture of each camera is divided into nine subapertures (channels) arranged in a 3 × 3 grid. The desired field of view of the system is 10°, and the wavelength range of operation is 9–11 μm. In the TOMBO system, each channel consists of a convex lenslet as shown in Fig. 1. The corresponding lenslet in each subaperture is shifted by a subpixel amount with respect to the centers of the subapertures, with an exception of the lenslet in the center. These shifts help create nonredundant subaperture images from which the single high-resolution image can be ob-
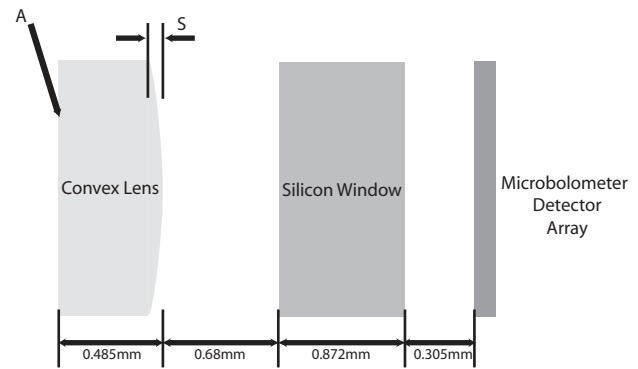

Fig. 1. Optical layout of one channel of the multichannel LWIR imaging systems. The surface A contains the phase grating for the coded PSF system. S denotes the sag of the convex element. The optical system thickness is 2.3 mm.

tained. The shift in each subaperture is 70 μm, and this corresponds to 2 1/3 pixels of the detector being used in the system (as shown in Fig. 2).

The design parameters for the optical system were optimized for the spot size over the wavelength range of interest. The resulting optical system thickness (distance between the front surface of the first element to the detector array) is 2.3 mm, as shown in Fig. 1. Each convex lenslet on the array has a radius of curvature of −3.627 mm and a sag(S) of 50.1 μm (which is the thickness of the microlens element, as indicated in Fig. 1) and is manufactured with silicon. In the coded PSF system, in addition to the convex lenslet in each channel (as in the TOMBO system), a phase grating is used to diffract the image. This grating is located on surface A in Fig. 1. The grating
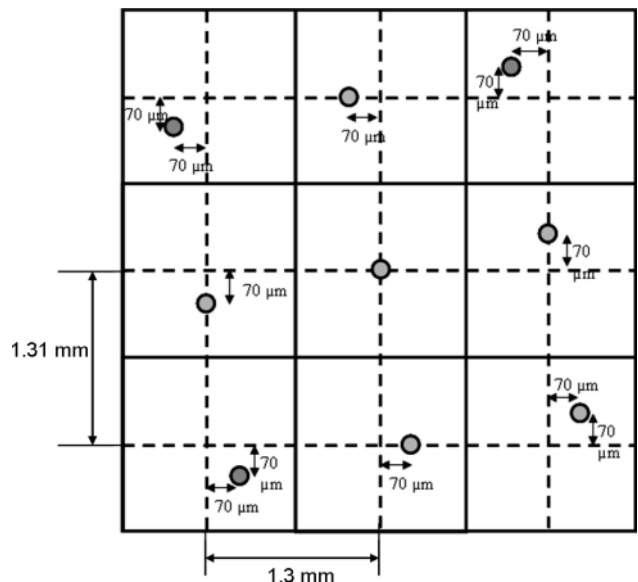

Fig. 2. Positions of the lenslets in each subaperture of the TOMBO IR system. The centers of the lenslets (indicated by the circles) are shifted by 70 μm in different directions with respect to the centers of the subapertures. The pitch of the lenslets in the horizontal direction is 1.3 mm and that in the vertical direction is 1.31 mm as shown.
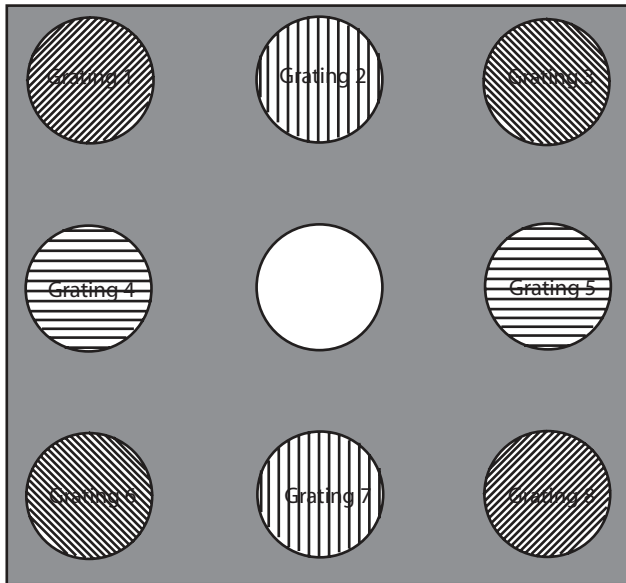
Fig. 3. Phase grating array used in the coded PSF system. The orientation of the gratings in each of the subapertures is different. The period of gratings 1, 3, 6, and 8 is 286.2 μm and that of gratings 2, 4, 5, and 7 is 401.6 μm. The center subaperture does not have a grating associated with it.

period, as well as its orientation in each of the subapertures, is different as shown in Fig. 3. The resulting image from each subaperture is therefore diffracted in a different direction. The shift associated with the -1 and $+1$ diffraction orders amounts to 80 μm on the detector array.

The spot diagram and the modulation transfer function (MTF) obtained from the two systems for a wavelength of 10 μm and different field angles are shown in Figs. 4 and 5, respectively. The polychromatic PSFs of the two systems are obtained experimentally by imaging an infrared point source and are shown in Fig. 6.

3. Fabrication Details

The lens arrays were fabricated on silicon wafers by use of a photoresist reflow and etching process. With this method hundreds of systems can be fabricated at the wafer scale simultaneously, making it an inexpensive process. Photoresist was first spun onto a silicon wafer. A mask with the lens pattern was then used to expose and define the lens footprints. The photoresist was developed after exposing and baking, leaving pillboxlike structures. These structures were melted, or reflowed, and then transfer etched into the silicon using an inductively coupled plasma reactive-ion-etching system. In the case of the TOMBO system optics, the wafers were then antireflection (AR) coated and diced.

For the coded PSF system, a diffractive pattern was created on the side of the wafer opposite to the lenses and aligned to them to form the phase gratings (surface A in Fig. 1). This was done by spinning photoresist on the wafer and using a front-to-back alignment system to register a mask with the diffractive
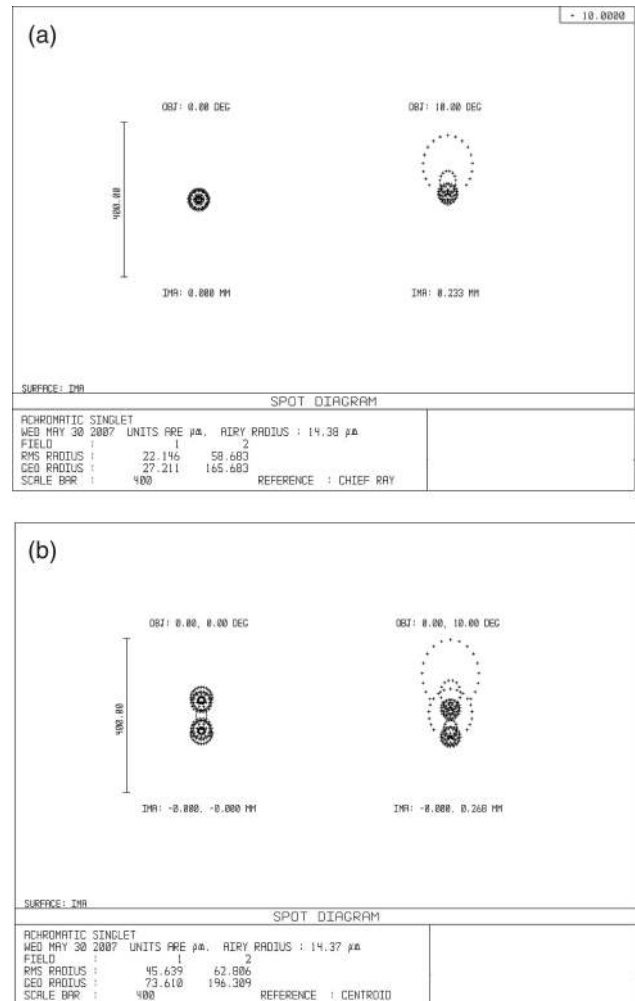

Fig. 4. (a) Spot diagram of the optical system of the TOMBO system and (b) coded PSF system for the wavelength of 10 μm at the field angles of 0° and 10°. The black circle represents the diffraction-limited spot. The resulting shift in the spots due to the diffractive element in the coded PSF system is 80 μm.

patterns to the refractive surface on the opposite side. The diffractive patterns were then exposed, developed, and transfer etched into the silicon surface. The wafers were then AR coated and diced.

4. System Description

The lens system was precisely positioned to place the detector array at the appropriate distance from the refractive lens array. The position of the lens is kept fixed by fabricating an enclosure to hold the lens array and incorporating it into the lens mount of the original camera. The optical channels were not isolated from one another and any cross talk was removed in postprocessing. The three camera systems are shown in Fig. 7. An α-silicon-based microbolometer array obtained from a commercial infrared camera (Thermal Eye 3500AS, manufactured by L-3 Communications) formed the detector plane. The size of the array is 120×160 pixels with a pitch of 30 μm. The conventional imaging lens system that we used has an optical system thickness of 26 mm. This lens

Fig. 7. Three IR camera systems—from left to right, the coded PSF system, the conventional single-aperture system, and the TOMBO system.

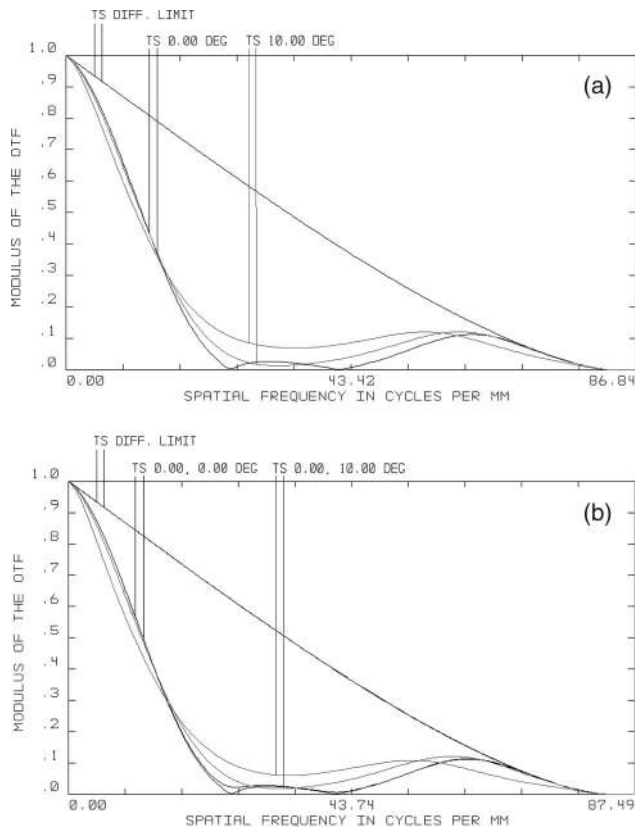
Fig. 5. Modulation transfer function of (a) the optical system of the TOMBO system and (b) the coded PSF system for the wavelength of 10 μm at the field angles of 0° and 10°. For each field angle, the tangential (T) and sagittal (S) MTFs are shown. Also shown is the diffraction-limited MTF.

system is replaced by the convex lenslet array in two of the cameras (Fig. 8). A bandpass filter on the silicon window of the wafer sealed detector package serves, along with the tuned cavity absorber on the surface of the detector, to limit the optical response of

the detector to the 8–14 μm spectral range. The camera was controlled through software by a computer that was also used to capture the raw data from the detector array. Raw images obtained from the multichannel systems are shown in Fig. 9. The nine low-resolution images are generated by the microlenses. The apparent blur in the subaperture images from the coded PSF system [Fig. 9(b)] is due to diffraction from the phase grating array.

5. Image Reconstruction

We now describe the system model as well as the reconstruction algorithms that we used for each multiaperture imaging system.

A. System Model

A measurement from the multichannel imaging systems can be modeled as [9] $x_k = H_k f + n_k$, $k = 1, 2, \ldots, 9$, where H_k is the system matrix representing the transformation from the scene f to the measurement x_k in the kth channel and n_k represents the noise present in the channel. By concatenating the set of measurements into a single array x and the
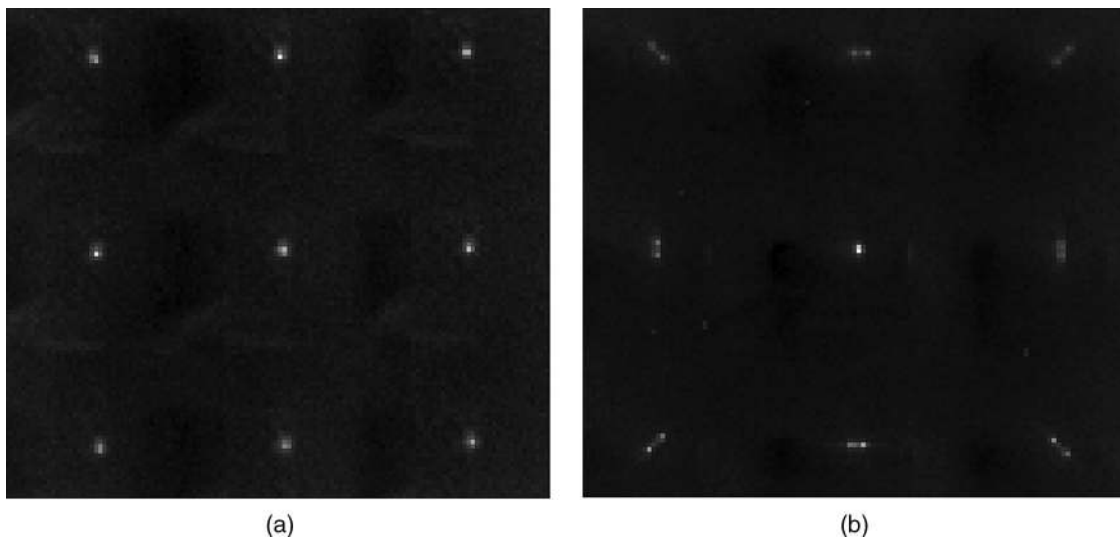

Fig. 6. Experimentally obtained point-spread functions of (a) the TOMBO system and (b) the coded PSF system. The shifts caused by the phase grating array is evident in (b).
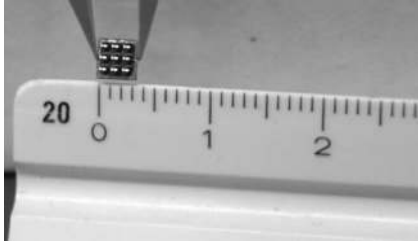
Fig. 8. 3×3 convex microlens array used in the cameras.

noise observations into an array n and letting H be a matrix composed of the nine system matrices from all the channels vertically concatenated, we have the system model

$$x = Hf + n. \tag{1}$$

From the formulation above, it is clear that reconstruction of the high-resolution image from the low-resolution measurements essentially involves an inversion of the operator matrix H. In the TOMBO system, the system matrix H comprises the shifting, blurring, and downsampling operations in each of the subapertures. In the coded PSF system, the system matrix includes the diffraction-induced shifts by the phase grating elements in addition to the blurring and downsampling in each of the subapertures.

It is an ongoing research effort to characterize the noise in the system, which originates from a variety of sources. We explore various reconstruction algorithms, assuming different noise models. Among these algorithms, the wavelet-based expectation maximization (EM) algorithm (designed assuming a Gaussian noise model [10]) performs well on the TOMBO system and the Richardson–Lucy (R–L) algorithm (designed assuming a Poisson noise model [11]) works well on the coded PSF system. In our experiments, the least gradient (LG) algorithm performs well on both systems, especially in distributed scenes. Each of these algorithms is described below.

B.   TOMBO Image Reconstruction

We explore two algorithms for the reconstruction of a single high-resolution image from the nine low-resolution shifted images in the TOMBO system—a linear approach called the LG method and a nonlinear wavelet-based EM approach.

1.   Least Gradient Algorithm

The LG or minimum variance algorithm solves the image reconstruction optimization problem for the image that is varying the least in the gradient:

$$f_{\mathrm{LG}} = \arg\min_f \gamma(f) = \|\nabla f\|_2 \tag{2}$$

such that $Hf = x$, where ∇ denotes the discrete gradient operator. When discretized over equispaced samples of a signal, the gradient may be the backward difference $\nabla_k f = f_k - f_{k-1}$, the forward difference, or the central difference. In matrix expression, ∇ is an $(n - 1) \times n$ bidiagonal matrix:

$$\nabla = \begin{bmatrix} -1 & 1 & 0 & \cdots & 0 \\ 0 & -1 & 1 & \cdots & 0 \\ \vdots & \vdots & \ddots & \ddots & \vdots \\ 0 & 0 & \cdots & -1 & 1 \end{bmatrix}.$$

For images, the two-dimensional operator $\nabla \otimes \nabla$ is required, where $\otimes$ denotes the Kronecker or tensor product of two matrices. We get a solution to the LG problem (2), in two steps. First, we obtain a solution f_p to the linear equation $Hf = x$. The general solution to this linear equation can then be described as $f = f_p - Nc$, where N spans the null space of H and c is an arbitrary coefficient vector. The problem (2) is reduced to the unconstrained linear least-squares problem:

$$f_{LG} = \arg\min_c \|\nabla(Nc - f_p)\|_2.$$

The solution to the LG problem (2) can be expressed as follows:
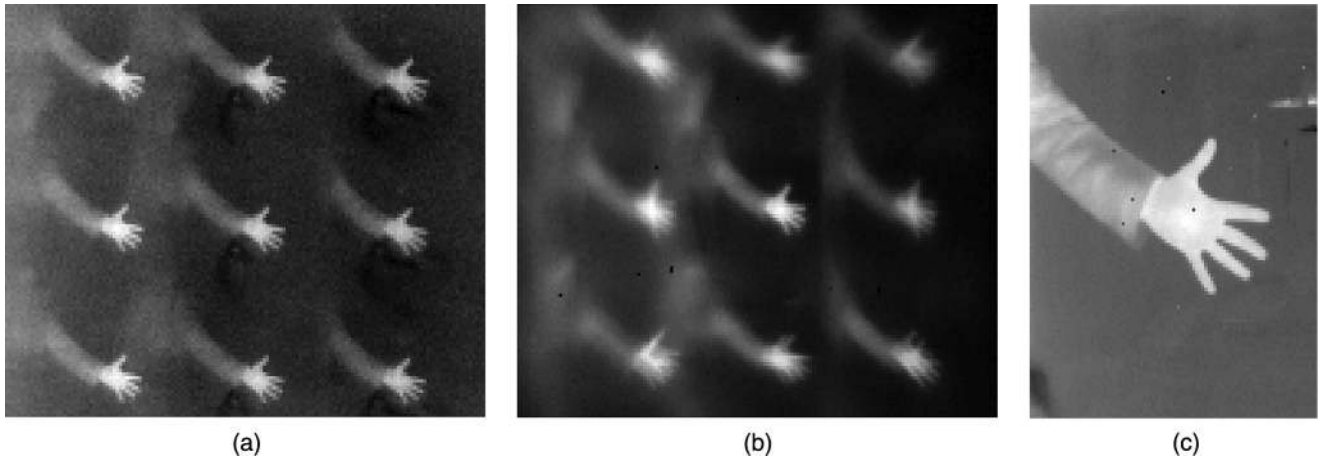

Fig. 9.   Raw images obtained from the IR cameras: (a) TOMBO camera, (b) coded PSF camera, and (c) conventional camera.
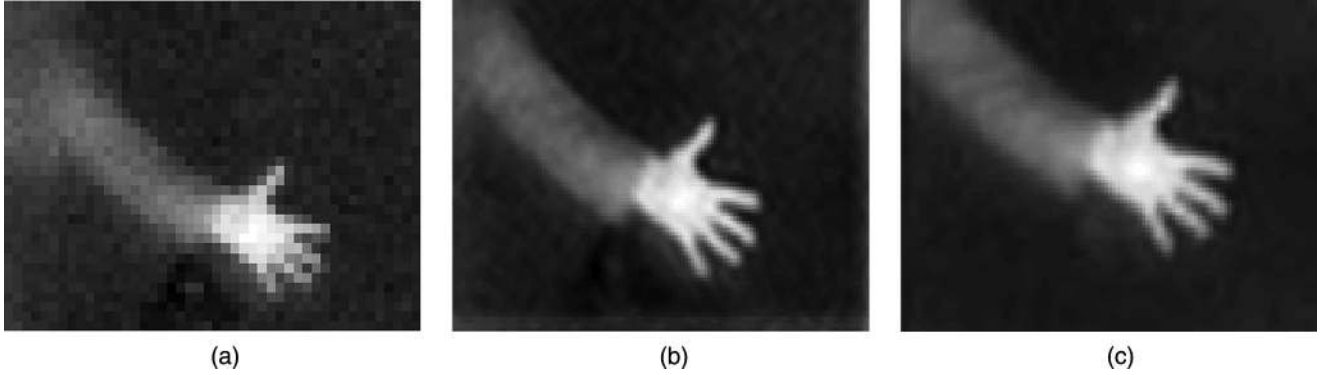
Fig. 10. (a) Image obtained from a single lenslet of the TOMBO camera, (b) image after reconstruction using the LG technique on the TOMBO image, and (c) image after reconstruction using the wavelet-based EM technique on the TOMBO image.

$$f_{LG} = f_p - N(N^T\nabla^T\nabla N)^{-1}(\nabla N)^T\nabla f_p, \qquad (3)$$

assuming that the ∇N is of full column rank. For separable problems, the null space of a Kronecker product is the Kronecker product of the null spaces of the terms.

2. Wavelet-Based Expectation Maximization

We also use an iterative wavelet-based EM algorithm to reconstruct a single high-resolution image from the nine low-resolution TOMBO images. The algorithm is based on one proposed by Figueiredo and Nowak [12], who approached the image deconvolution problem with a method that combines the efficient image representation by the discrete wavelet transform (DWT) and the diagonalization of the convolution operator obtained in the Fourier domain. The algorithm alternates between a linear filtering expectation step (E-step) and a DWT-based maximization step (M-step), which performs image denoising.

The system matrix H is known based on design parameters of the optical system. The observation model shown in Eq. (1) can be expressed with respect to the DWT coefficients θ, where $f = W\theta$ and W denotes the inverse DWT operator [13]: $x = HW\theta + n$.

The noise in the observation model (denoted by n) can be decomposed into two Gaussian terms (one of which is nonwhite). The Gaussian observation model can now be expressed as

$$x = \underbrace{H(W\theta + \alpha n_1)}_{z} + n_2,$$

where α is a positive parameter, and n_1 and n_2 are independent zero-mean Gaussian noises with covariances $\Sigma_1 = I$ and $\Sigma_2 = \sigma^2 I - \alpha^2 HH^T$, respectively. We treat z as the missing data and use the EM algorithm to estimate θ.

Using these formulations, the EM algorithm provides an estimate $f^{(i)}$ at the ith iteration by alternately applying the E- and the M-steps defined as follows:

E-step: This step updates the estimate of the missing data using the relation

$$\hat{z}^{(i)} = E[z|x, \, \hat{\theta}^{(i)}].$$

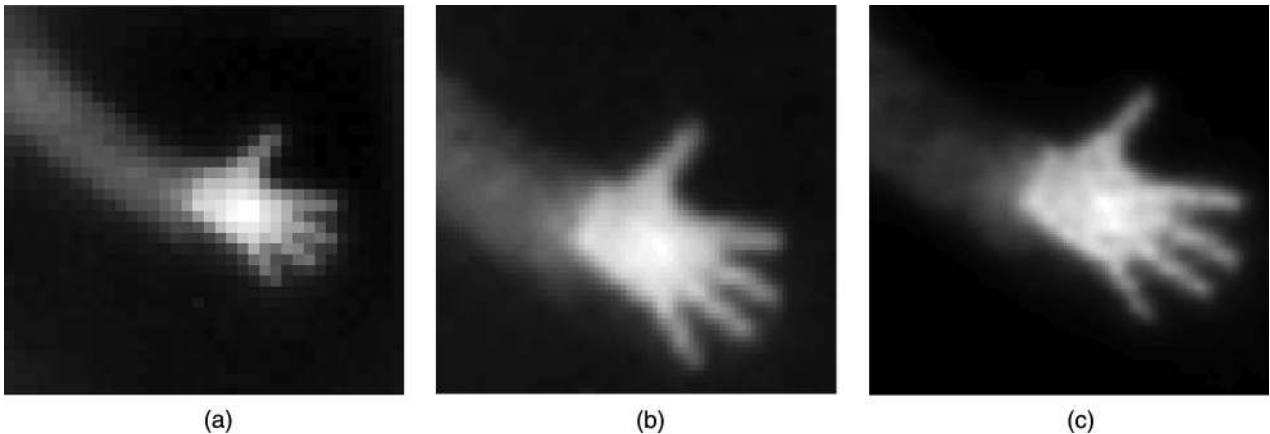In the case of Gaussian noise, this can be reduced to a Landweber iteration [14]:

Fig. 11. (a) Image obtained from a single lenslet of the coded PSF camera, (b) image obtained after reconstruction using the LG algorithm on the coded PSF image, and (c) image after reconstruction using the R–L technique on the coded PSF image.

Fig. 12. Frame wound with heating wires placed at an angle to observe the modulation from the three cameras.

$$\hat{z}^{(i)} = \hat{f}^{(i)} + \frac{\alpha^2}{\sigma^2} H^T\big(x - H\hat{f}^{(i)}\big).$$

Here, computing $\hat{z}^{(i)}$ simply involves applications of the operator H and its adjoint.

M-step: This step updates the estimate of the high-resolution image f. This constitutes updating the wavelet coefficient vector θ according to

$$\hat{\theta}^{(i+1)} = \arg\min_{\theta}\left\{\frac{\|W\theta - \hat{z}^{(i)}\|_2^2}{2\alpha^2} + \text{pen}(\theta)\right\}$$

and setting $\hat{f}^{(i+1)} = W\hat{\theta}^{(i+1)}$. This optimization can be performed using one of several wavelet-based denoising procedures. For example, under an independent and identically distributed Laplacian prior, $\text{pen}(\theta) = -\log p(\theta) \propto \tau\|\theta\|_1$ (where $\|\theta\|_1 = \sum_p |\theta_p|$ denotes the l_1 norm), is obtained by applying a soft-threshold function to the wavelet coefficients of $\hat{z}^{(i)}$. For the reconstructions presented in this paper, we applied a similar denoising method described by Figueiredo and Nowak [15].

Figure 10 shows the image obtained from a single lenslet of the TOMBO camera, after performing the LG reconstruction on the raw data [Fig. 9(a)] and using the wavelet EM algorithm. It is clear from the reconstructions that there is an improvement in the resolution from the single lenslet.

C. Coded PSF Image Reconstruction

To reconstruct a single high-resolution image from the multiple low-resolution images, we try two approaches—a linear LG algorithm and a R–L deconvolution algorithm.

1. *Least Gradient Algorithm*
The LG technique used to reconstruct a high-resolution image with the coded PSF system is similar to the one described above for the TOMBO system. Here, we account for the unique PSFs in each of the subapertures by incorporating them in the system matrix H. Figure 11(a) shows an image obtained from a single lenslet and Fig. 11(b) shows the image reconstructed after using the LG algorithm.

2. *Richardson–Lucy Algorithm*
We use an iterative R–L-based deconvolution [16,17] algorithm based on knowledge of the PSF of the system. The PSF defines the transformation matrix H in Eq. (1). From the sensor measurements x, the $(k + 1)$th update of the estimate of the scene is obtained from the kth estimate by the following R–L step:

$$\hat{f}^{(k+1)} = \hat{f}^{(k)} \odot H^T\left(\frac{x}{H\hat{f}^{(k)}}\right),$$

where $\odot$ indicates an elementwise multiplication. Figure 11(c) is the reconstructed image obtained after performing the R–L deconvolution on the measurements [Fig. 9(b)]. A resolution improvement in the reconstructions over the single lenslet image is clear.

6. **Performance Comparison**
We observe the performance of the two multiaperture IR cameras compared with the conventional single-aperture IR camera. In particular, we observe the
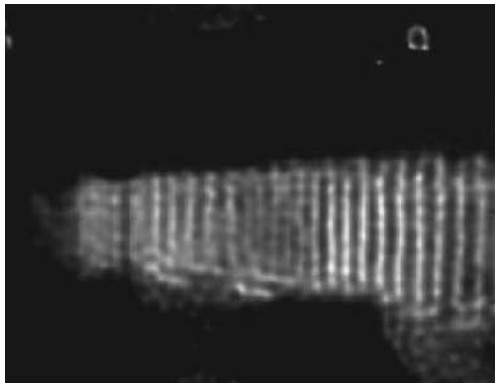
(a)
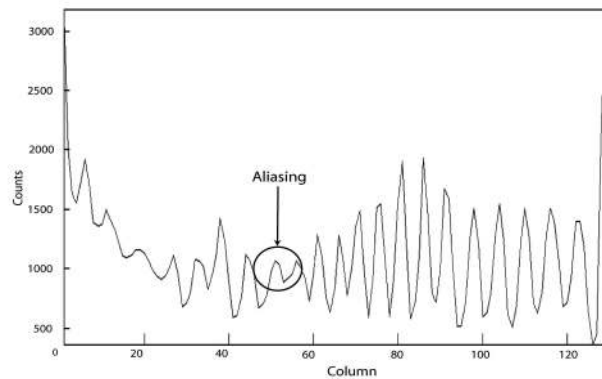
(b)

Fig. 13. (a) Reconstruction of the image of the wire frame from the TOMBO system and (b) the corresponding modulation obtained by plotting the intensity across all columns from one selected row from the reconstructed image.
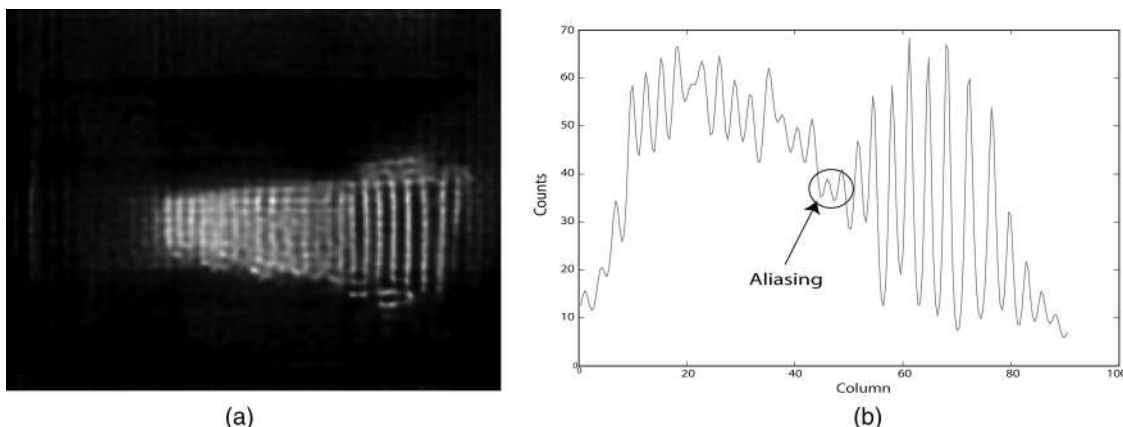
Fig. 14. (a) Reconstruction of the image of the wire frame from the coded PSF system and (b) the corresponding modulation obtained by plotting the intensity across all columns from one selected row from the reconstructed image.

modulation characteristics as well as the two-point (Rayleigh) resolution of these systems. We use the wavelet-based EM algorithm for the TOMBO image reconstructions and the R–L algorithm for the coded PSF image reconstructions.

A. Modulation

We measured the modulation of the camera systems with an infrared wire-frame chart. This was built using pipe heating wires coiled within a frame in such a way as to space the lines 2 in. (5 cm) apart. The spatial frequency was varied by tilting the frame with respect to the cameras as shown in Fig. 12. At regions of the wire frame close to the camera, the spatial frequency as seen by the camera is low and it progressively increases as the distance of the frame and the camera increases. The modulation is viewed by plotting the intensity profile across all columns from one selected row from the reconstructed image of the wire frame.

The reconstructions and the corresponding plots of the modulation for the three camera systems are shown in Figs. 13–15. The direction of increasing spatial frequency is from right to left (based on the placement of the cameras with respect to the wire frame). From the modulation plots it can be seen that the multiaperture systems perform well at lower spatial frequencies, but as the spatial frequency increases, the individual wires on the frame become less resolvable. Aliasing from each of the systems at higher spatial frequencies is clear and they have been indicated in the plots.

B. Two-Point Resolution

The two-point resolution for each of the camera systems was determined by using incense sticks as point sources. These were setup at a distance of 75 in. (190 cm) from the cameras, 3 in. (8 cm) apart from each other. By bringing the sticks closer together and observing the images obtained from the cameras (the conventional camera image and the reconstructed images from the multichannel cameras), the two-point resolution of the three systems can be measured. Plots from the three systems, along the line in the reconstructed image where the two point sources were located, are shown in Fig. 16. Using these plots, the two-point resolutions of the three cameras were determined to be 0.035, 0.025, and 0.02 rad for the
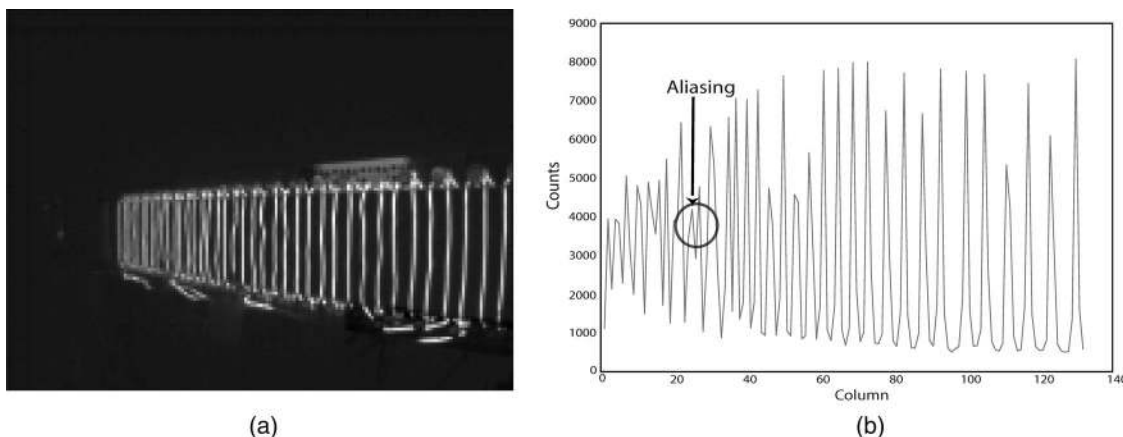

Fig. 15. (a) Image of the wire frame obtained from the conventional IR camera and (b) the corresponding modulation obtained by plotting the intensity across all columns from one selected row from the image.
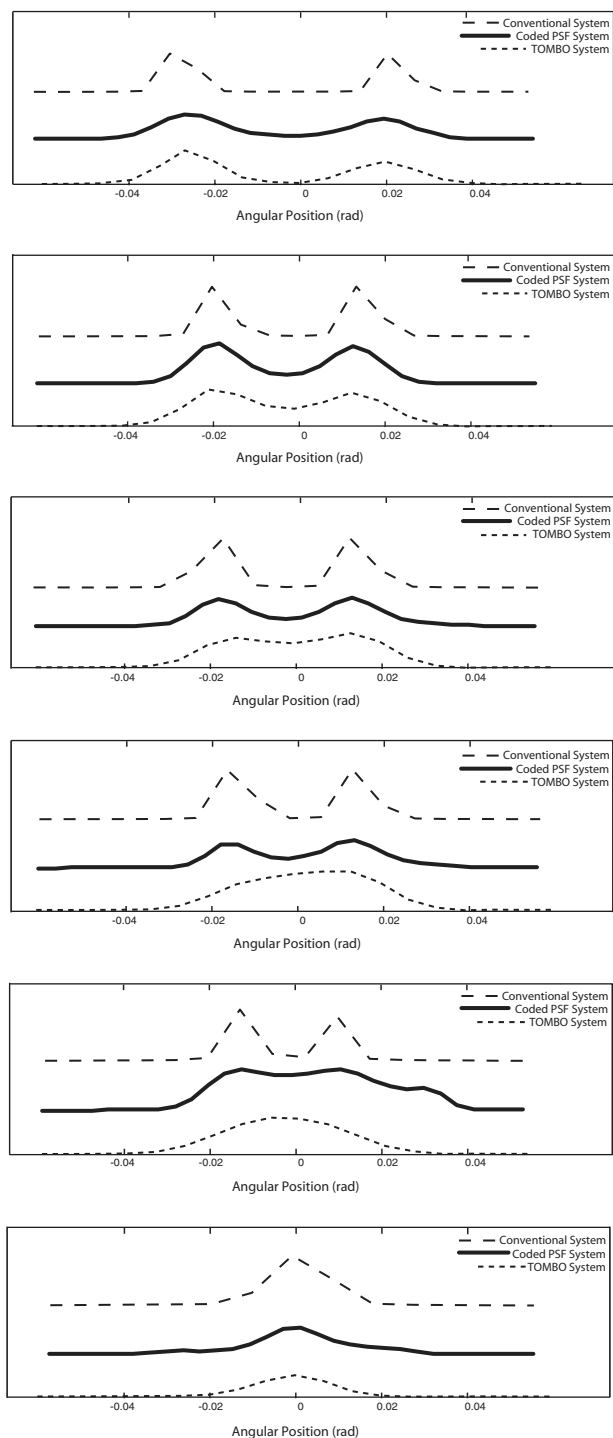
Fig. 16. Determination of two-point resolution of the cameras. Plots of the intensity along the row containing the point sources in the reconstructed image as the sources are brought closer together.

TOMBO system, coded PSF system, and conventional camera, respectively.

7. Conclusions

A reduction in optical system thickness of infrared cameras could be obtained through multichannel sampling. We designed and developed two ultrathin camera systems by replacing the conventional optics with a 3 × 3 lenslet array, and as a result the system thickness was reduced by a factor of more than 10. We developed the algorithms to reconstruct a single high-resolution image from the multiple low-resolution images and observed the modulation and two-point resolution performance of the three camera systems.

In the tests that were performed, the TOMBO system had better image quality than the coded PSF system. However, the coded PSF system had better two-point resolution performance than the TOMBO system. The use of nonlinear algorithms for the reconstructions helped improve the performance but also resulted in a degradation of image quality. The coded PSF system has a phase grating array that further degrades image quality. The multichannel systems were unable to match the performance of the conventional system in the modulation experiments. In the two-point resolution test, the coded PSF system achieves performance close to the conventional system. The optics that were fabricated did not meet the exact specifications required by the design. There were inaccuracies (misalignments in the subpixel shifts) during the assembly of the optics with the focal plane array. These misalignments were estimated using image registration techniques, which were effective in improving the image quality.

Work is currently under way in the implementation of a next-generation system that has better-quality optics, incorporates additional corrective optics in the optical system, and utilizes a more effective system assembly technique. It is expected that the system will show much better image quality than the first-generation system and a more comparable performance with a conventional system. This work paves the way for ultrathin light and low-cost IR cameras for applications that demand small form factors, such as night vision visors for soldiers in the field.

References

1. S. Ogata, J. Ishida, and T. Sasano, "Optical sensor array in an artificial compound eye," Opt. Eng. **33**, 3649–3655 (1994).
2. J. S. Sanders and C. E. Halford, "Design and analysis of apposition compound eye optical sensors," Opt. Eng. **34**, 222–235 (1995).
3. K. Hamanaka and H. Koshi, "An artificial compound eye using a microlens array and its application to scale invariant processing," Opt. Rev. **3**, 264–268 (1996).
4. G. A. Horridge, "Apposition eyes of large diurnal insects as

organs adapted to seeing," Proc. R. Soc. London **207,** 287–309 (1980).

5. J. Tanida, T. Kumagai, K. Yamada, S. Miyatake, K. Ishida, T. Marimoto, N. Kondou, D. Miyazaki, and Y. Ichioka, "Thin observation module by bound optics (TOMBO): concept and experimental verification," Appl. Opt. **40,** 1806–1813 (2001).

6. K. Nitta, R. Shogenji, S. Miyatake, and J. Tanida, "Image reconstruction for thin observation module by bound optics by using the iterative backprojection method," Appl. Opt. **45,** 2893–2900 (2006).

7. A. V. Kanaev, D. A. Scribner, J. R. Ackerman, and E. F. Fleet, "Analysis and application of multiframe superresolution processing for conventional imaging systems and lenslet arrays," Appl. Opt. **46,** 4320–4328 (2007).

8. E. Dowski and K. Kubala, "Reducing size, weight, and cost in a LWIR imaging system with wavefront coding," Proc. SPIE **5407,** 66–73 (2004).

9. R. Willett, I. Jermyn, R. Nowak, and J. Zerubia, "Wavelet-based superresolution in astronomy," in *Proceedings of Astronomical Data Analysis Software and Systems* (Astronomical Society of the Pacific, 2003), Vol. 314, p. 107.

10. M. Shankar, R. Willett, N. P. Pitsianis, R. Te Kolste, C. Chen, R. Gibbons, and D. J. Brady, "Ultra-thin multiple-channel LWIR imaging systems," Proc. SPIE **6294,** 629411 (2006).

11. T. J. Schulz, "Multiframe blind deconvolution of astronomical images," J. Opt. Soc. Am. A **10,** 1064–1073 (1993).

12. M. Figueiredo and R. Nowak, "An EM algorithm for wavelet-based image restoration," IEEE Trans. Image Process. **12,** 906–916 (2003).

13. S. Mallat, *A Wavelet Tour of Signal Processing* (Academic, 1998).

14. L. Landweber, "An iteration formula for Fredholm integral equations of the first kind," Am. J. Math. **73,** 615–624 (1951).

15. M. Figueiredo and R. Nowak, "Wavelet-based image estimation: an empirical Bayes approach using Jeffreys' noninformative prior," IEEE Trans. Image Process. **10,** 1322–1331 (2001).

16. W. H. Richardson, "Bayesian-based iterative method of image restoration," J. Opt. Soc. Am. **62,** 55–59 (1972).

17. L. B. Lucy, "An iterative technique for the rectification of observed distributions," Astron. J. **7,** 745–754 (1974).